International Journal of Heat and Mass Transfer 52 (2009) 385–395

Contents lists available at ScienceDirect

International Journal of Heat and Mass Transfer

journal homepage: www.elsevier.com/locate/ijhmt

Heat and mass transfer analysis of a suspension of reacting particles subjected to concentrated solar radiation – Application to the steam-gasification of carbonaceous materials

A. Z'Graggen [a], A. Steinfeld [a,b,*]

[a] Department of Mechanical and Process Engineering, ETH Zurich, 8092 Zurich, Switzerland
[b] Solar Technology Laboratory, Paul Scherrer Institute, 5232 Villigen, Switzerland

ARTICLE INFO

Article history:
Received 3 July 2007
Received in revised form 7 April 2008
Available online 23 July 2008

Keywords:
Radiation
Particulate
Thermochemistry

ABSTRACT

A chemical reactor for the steam-gasification of carbonaceous materials (e.g. coal, coke, biomass) using high-temperature solar process heat is modeled by means of a two-phase formulation that couples radiative, convective, and conductive heat transfer to the chemical kinetics for polydisperse suspensions of reacting particles. The governing mass and energy conservation equations are solved by applying advanced Monte–Carlo and finite-volume techniques with smoothing and underrelaxation. Validation is accomplished by comparing the numerically calculated temperatures, product compositions, and chemical conversions with the experimentally measured values obtained from testing a 5 kW solar reactor prototype in a high-flux solar furnace. A unique feature of the reactor concept is that the gas-particle flow is directly exposed to concentrated solar radiation, providing efficient radiative heat transfer to the reaction site for driving the high-temperature highly endothermic process.

1. Introduction

Hybrid solar/fossil endothermic processes, in which concentrated solar radiation is used exclusively as the energy source of high-temperature process heat, offer a viable route for fossil fuel decarbonization and create a transition path towards solar hydrogen [1]. An important example of such hybridization is the endothermic steam-gasification of carbonaceous materials (coal, coke, biomass, etc.) to synthesis gas (syngas). The advantages of supplying solar energy for process heat are fourfold: (1) the calorific value of the feedstock is upgraded; (2) the gaseous products are not contaminated by the by-products of combustion; (3) the discharge of pollutants to the environment is reduced, and (4) the need for the energy-intensive processing of pure oxygen is eliminated [2]. A solar chemical reactor was designed and a 5 kW prototype was fabricated and experimentally demonstrated for steam-gasification of petroleum coke (petcoke) in a high-flux solar furnace [3,4]. This reactor features a continuous vortex-flow of steam laden with petcoke particles, confined to a cavity receiver and directly exposed to concentrated solar radiation. The direct irradiation of the particle suspension provided an efficient means of heat transfer directly to the reaction site where the energy is needed; bypassing the limitations imposed by conductive heat transport through the reactor walls.

The present work is focused on the modeling aspects of such a high-temperature chemical reactor, with emphasis on the fundamental analysis of heat and mass transfer in a directly irradiated suspension of reacting particles. Radiative heat transfer in a polydisperse particulate medium is solved by the forward Monte–Carlo (MC) method based on the pathlength approach with ray-redirection using equivalent monodisperse diameters [5]. Previous pertinent MC modeling studies include pulverized coal furnaces [6] and solar reactors for coal gasification [7–10] and CH_4 decomposition [11]. The mass and energy conservation equations for a two-phase fluid flow coupling radiative, conductive, and convective heat transfer with the reaction kinetics are solved iteratively by finite volume technique with Gaussian kernel smoothing and adaptive underrelaxation. The scheme developed here is able to deal with concentrated thermal radiation input, polydisperse particulate media with spectral and directional optical properties, and temperature-dependent chemical kinetics and fluid properties. Validation is accomplished by comparing numerical and experimental results.

2. Polydisperse particle suspension

The two-phase medium considered is composed of a solid particulate polydispersion suspended in a gas mixture. The particle suspension is modeled as a non-gray absorbing, emitting,

* Corresponding author. Address: Department of Mechanical and Process Engineering, ETH Zurich, 8092 Zurich, Switzerland. Tel.: +41 44 6327929; fax: +41 44 6321065.
E-mail address: aldo.steinfeld@eth.ch (A. Steinfeld).

0017-9310/$ - see front matter © 2008 Elsevier Ltd. All rights reserved.
doi:10.1016/j.ijheatmasstransfer.2008.05.023

Nomenclature

A_s	surface of solid particles (m^2)
c_p	specific heat capacity (J/(kg K))
D	particle diameter (m)
D_c	diffusion coefficient (m^2/s)
E_A	activation energy
$e_{\lambda b}$	Planck's blackbody spectral emissive power ($W/(m^2\ \mu m)$)
f	particle size distribution function
f_V	solid volume fraction
h	enthalpy (J/kg)
h_c	convective heat transfer coefficient ($W/(m^2\ K)$)
i	radiation intensity ($W/(m^2\ sr)$)
K	kinetic rate constant
k	thermal conductivity (W/(m K))
k_0	kinetic frequency factor
L	characteristic length (cm)
M	molar mass (kg/mol)
m	mass (kg)
N_p	number of particles
Nu	Nusselt number
n	number of moles
p	pressure (Pa)
$Q_{a,s,ext}$	absorption, scattering and extinction efficiencies for a single sphere
$\dot{Q}_{solar}$	incident solar radiation (W)
$\dot{q}_{solar}$	incident solar radiative flux (W/m^2)
r	radial coordinate (m)
r_i	mass specific reaction rate of specie i (mol/(g s))
R	universal gas constant (J/(mol K))
R_i	volumetric reaction rate of specie i ($kg/(m^3\ s)$)
S	cross sectional area (m^2)
t	time (s)
T	temperature (K)
U	overall heat transfer coefficient ($W/(m^2\ K)$)
u	velocity (m/s)
V	volume (m^3)
x	axial coordinate (m)
X_C	carbon conversion
X_{H_2O}	steam conversion
Y_i	mass fraction of species i
y_i	molar fraction of species i

Greeks

β	extinction coefficient (m^{-1})
ε	emissivity
η	particle effectiveness factor
κ	absorption coefficient (m^{-1})
μ	dynamic viscosity (kg/(m s))
ρ	density (kg/m^3)
Φ	scattering phase function
ϕ	energy source term (W/m^3)
σ	Stefan–Boltzmann constant 5.67051×10^{-8} ($W/(m^2\ K^4)$)
σ_s	scattering coefficient (m^{-1})
τ	relaxation time (s)
ξ	size parameter

Subscripts

b	blackbody
g	gaseous phase
gr	graphite
i	species
in	inlet
s	solid phase
λ	spectral

and scattering participating medium subjected to concentrated thermal radiation. The initial particle diameters are in the range 1–100 μm. Both solid and gas phases are involved in the heterogeneous chemical reaction taking place predominantly on the outer surface of the solid particles and, to some extent, on the inner porous surface of the particles. Typical radiative equilibrium temperatures are in the range 1500–1800 K. As the gasification reaction progresses and the solid particles shrink, the thermal and optical properties of the particle suspension vary.

Representative relaxation times are compared for assessing the relative importance of the different modes of heat transfer, namely conduction, convection, and radiation. The reference time scale for the fluid flow, $\tau_{flow} = L/u$, equals 0.1 s, with $L = 1$ cm as the characteristic length. For conductive heat transfer inside a spherical particle, the relaxation time of its core temperature with respect to a sudden change in its surface temperature [12], $\tau_{conduction} = \rho_s c_{p,s} D^2/(4k_s)$, is 10 to 10^5 times shorter than τ_{flow} for 100 to 1-μm diameter particles, respectively. Uniform temperature is therefore assumed for a single particle. For convective heat transfer across a stationary sphere, $Nu = 2$ [12]. The relaxation time of the temperature of a spherical particle submerged in a fluid at a different temperature [12], $\tau_{convection} = \rho_s c_{p,s} D^2/(12k_g)$, is comparable to τ_{flow} for 100 μm particles. The energy conservation equation is therefore solved for each phase separately. For radiative heat transfer, the relaxation time of the particle temperature with surroundings at T_0, $\tau_{radiation} = \rho_s c_{p,s} D/(24\sigma\varepsilon T_0^3)$, is 1 to 3 orders of magnitude smaller than τ_{flow}. The temperature field is therefore mainly influenced by the local divergence of the radiative flux and only marginally by the heat transported by advection.

The polydisperse medium is characterized by its population density, i.e. the particle size distribution function f describing the number of particles found in an infinitesimal interval around diameter D. For a sample containing a discrete number of particles N_p with diameters D_i,

$$f(D) = \frac{1}{N_p}\sum_{i=1}^{N_p}\delta(D - D_i) = \frac{1}{N_p}\sum_{i=1}^{N_p} w(D - D_i, \triangle D) \tag{1}$$

where the Dirac function δ is substituted for a symmetric kernel function w around 0 with bandwidth ΔD and with $\int_0^\infty w \cdot dD = 1$. For simplification, the polydisperse medium can be described by a set of equivalent monodisperse diameters defined as

$$D_{pq} = \left(\frac{\int_0^\infty f(D)D^p\,dD}{\int_0^\infty f(D)D^q\,dD}\right)^{\left(\frac{1}{p-q}\right)} \tag{2}$$

where p and q are integer numbers between 0 and 3. D_{30}, D_{31}, D_{32} are applied for volume-based, volume-to-diameter-ratio based, and volume-to-surface-ratio based phenomena, respectively.

3. Governing equations

The solid particles are assumed to be entrained in the gas phase, as justified by the Stokes number in the range of 10^{-2}–10^{-6}. Conduction and diffusion in the flow direction are neglected, as justified by the Peclet numbers for conduction ($Pe = uL/\alpha$) and for

diffusion ($Pe = uL/D_c$) in the order of 10^2. Steady-state mass conservation for the mixture is then expressed by:

$$\nabla \cdot (\rho \cdot \mathbf{u}) = 0 \tag{3}$$

and for a single specie i by:

$$\nabla \cdot (\rho Y_i \cdot \mathbf{u}) = R_i \tag{4}$$

where R_i denotes the volumetric rate of production/consumption of specie i. Steady-state energy conservation for the solid phase yields:

$$\nabla \cdot (\rho h \cdot \mathbf{u}) = \phi_{\text{radiation}} - \phi_{\text{convection}} - \phi_{\text{chemistry}} \tag{5}$$

where the radiation source $\phi_{\text{radiation}}$ is given by the negative divergence of the radiative flux $-\nabla \cdot \mathbf{q}_r$, the convection source $\phi_{\text{convection}}$ is given by the convective heat exchange between the two phases, and the chemistry source $\phi_{\text{chemistry}}$ is given by the enthalpy change during the chemical transformation. Steady-state energy conservation for the gas phase yields,

$$\nabla \cdot (\rho h \cdot \mathbf{u}) = \phi_{\text{convection}} + \phi_{\text{chemistry}} \tag{6}$$

Mean absorption coefficients of a typical product gas composition (CO, CO_2, H_2, H_2O) at 1 bar, calculated line-by-line using the HITEMP database [13], are approx. 0.06 and 0.006 m^{-1} for radiation emitted at 1800 and 5780 K, respectively. Absorption by the gas is therefore neglected vis-à-vis absorption by the particles.

3.1. Energy source for radiation

The divergence of the radiative flux is obtained from the difference between absorbed and emitted radiation,

$$-\nabla \cdot \mathbf{q}_r(S) = 4\pi \int_{\lambda=0}^{\infty} \kappa_\lambda(S) \left(\frac{1}{4\pi} \int_{\omega=0}^{4\pi} i_\lambda(S,\omega)\,\mathrm{d}\omega - i_{\lambda b}(S) \right) \mathrm{d}\lambda \tag{7}$$

where the radiative intensity i_λ is given by the equation for radiative transfer for a participating medium:

$$\frac{\mathrm{d}i_\lambda}{\mathrm{d}S} = -\beta_\lambda(S) i_\lambda(S) + \kappa_\lambda(S) i_{\lambda \mathrm{b}}(S) + \frac{\sigma_s \lambda(S)}{4\pi} \times \int_{\omega_i=0}^{4\pi} i_\lambda(S,\omega_i) \Phi_\lambda(\omega,\omega_i)\,\mathrm{d}\omega_i \tag{8}$$

For solid volume fractions $f_v < 10^{-3}$ considered in this study, the independent scattering regime is valid [14]. Continuum absorption, scattering, and extinction coefficients for the polydisperse medium are then calculated as a function of the corresponding properties for a single sphere [15]:

$$\{\kappa_\lambda, \sigma_{s,\lambda}, \beta_\lambda\} = \frac{3 f_V}{2} \cdot \frac{\int_0^\infty \{Q_{a,\lambda}, Q_{s,\lambda}, Q_{ext,\lambda}\} f(D) D^2\,\mathrm{d}D}{\int_0^\infty f(D) D^3\,\mathrm{d}D} \tag{9}$$

For size parameter $\xi = \pi D/\lambda > 5$, geometrical optics applies and Eq. (9) simplifies to:

$$\{\kappa_\lambda, \sigma_{s,\lambda}, \beta_\lambda\} = \frac{3}{2} \cdot \frac{f_V}{D_{32}} \cdot \{Q_{a,\lambda}, Q_{s,\lambda}, Q_{ext,\lambda}\} \tag{10}$$

For ξ in the range 1–10^3 considered in this study, Mie theory applies. $Q_{a,\lambda}$, $Q_{s,\lambda}$, $Q_{ext,\lambda}$ and the scattering phase function Φ_λ are calculated based on the complex refractive index of the solid material using the routine BHMIE [16] and, because of computational time constraints, using the Henyey–Greenstein approximation [17],

$$\Phi_\lambda(D,\theta_0) = \frac{1 - g_\lambda^2}{(1 + g_\lambda^2 - 2 g_\lambda \cdot \cos\theta_0)^{3/2}} \tag{11}$$

where the asymmetry factor $g_\lambda = 1/4\pi \cdot \int_{4\pi} \Phi_\lambda(D,\theta) \sin\theta\,\mathrm{d}\Omega$. The overall scattering phase function and the asymmetry factor for the polydisperse medium are calculated analogously to Eq. (9) [15],

$$\{\Phi_\lambda(\theta_0), g_\lambda\} = \frac{\int_0^\infty \{\Phi_\lambda(D,\theta_0), g_\lambda(D)\} \cdot Q_{s,\lambda} \cdot f(D) D^2\,\mathrm{d}D}{\int_0^\infty Q_{s,\lambda} \cdot f(D) D^2\,\mathrm{d}D} \tag{12}$$

3.2. Energy source for convection

Convective heat transfer between solid and gas phases is described by Newton's law of cooling [12]:

$$\phi_{\text{convection}} = \frac{\overline{(h_c \cdot A_s)}}{V}(T_s - T_g) = \frac{12 \cdot f_V \cdot k_g \cdot (T_s - T_g)}{D_{31}^2} \tag{13}$$

where $h_c = Nu \cdot k_g/D$ and $Nu = 2$ [12].

3.3. Energy source for chemistry

Species consumed or generated during the chemical reaction contributes to the enthalpy change, evaluated at the temperature of the originating phase:

$$\phi_{\text{chemistry}} = \sum_{i=1}^{n} h_i(T) \cdot R_i(T_s, Y_i, f) \tag{14}$$

Note that the enthalpy is related to temperature field by the implicit equation:

$$h = h_{\text{ref}} + \int_{T_{\text{ref}}}^{T} c_p \cdot \mathrm{d}T \tag{15}$$

where h_{ref} is the reference enthalpy at $T_{\text{ref}} = 273$ K.

3.4. Reaction kinetics

The steam-gasification of petcoke is selected as the modeled chemical process. The overall chemical conversion can be represented by the simplified net reaction:

$$CH_zO_y + (1-y)H_2O = \left(\frac{z}{2} + 1 - y\right)H_2 + CO \tag{16}$$

where z and y are the elemental molar ratios of H/C and O/C in petcoke, respectively. Table 1 lists the approximate main elemental chemical composition, the lower heating value (LHV), and elemental molar ratios of H/C and O/C for Petrozuata Delayed (PD) coke used in the experimental campaign. The kinetic model is based on the oxygen-exchange mechanism describing reversible O-transfer surface reactions followed by a unidirectional gasification step, and on reversible steam sorption as OH/H groups and irreversible surface chemistry [18]. A set of kinetic rate expressions of the Langmuir–Hinshelwood type are formulated to describe the formation and consumption of each gas species,

$$r_{H_2O} = \frac{-K_2 \cdot p_{H_2O} - K_2 K_3 \cdot p_{H_2O} p_{CO}}{1 + K_4 p_{CO_2} + K_5 p_{H_2O}} \tag{17}$$

$$r_{H_2} = -r_{H_2O} \tag{18}$$

$$r_{CO} = \frac{2K_1 \cdot p_{CO_2} + K_2 \cdot p_{H_2O} + -K_2 K_3 \cdot p_{H_2O} p_{CO}}{1 + K_4 p_{CO_2} + K_5 p_{H_2O}} \tag{19}$$

$$r_{CO_2} = \frac{-K_1 \cdot p_{CO_2} + K_2 K_3 \cdot p_{H_2O} p_{CO}}{1 + K_4 p_{CO_2} + K_5 p_{H_2O}} \tag{20}$$

$$r_C = -(r_{CO} + r_{CO_2}) = \frac{-K_2 \cdot p_{H_2O} - K_1 \cdot p_{CO_2}}{1 + K_4 p_{CO_2} + K_5 p_{H_2O}} \tag{21}$$

Table 1
Approximate main elemental chemical composition, low heating value, and elemental molar ratios of H/C and O/C for Petrozuata Delayed coke

Element	Molar fraction	Mass fraction
C	62.1	88.21
H	34.66	4.14
O	0.77	1.46
N	1.37	2.28
S	1.1	4.16
LHV/kJ kg^{-1}	35876	
H/C	0.5581	
O/C	0.0124	

Table 2
Arrhenius parameters of the kinetic rate constants for the steam gasification of petcoke [19]

	E_A/J mol^{-1}	k_0/s^{-1}
K_1	2.707×10^5	1.158×10^3
K_2	1.615×10^5	4.978×10^{-1}
K_3	-9.404×10^4	1.149×10^{-7}
K_4	7.068×10^3	4.033×10^{-8}
K_5	4.551×10^2	8.152×10^{-6}

r_i is the reaction rate of species i (i = H_2, H_2O, CO, CO_2 and C) for heterogeneous surface reactions, defined as:

$$-r_i = \frac{1}{m_C}\frac{dn_i}{dt} \tag{22}$$

where m_C is the mass of coke. K_1 to K_5 are lumped complex constants based on the elementary rate constants. Their temperature dependence is determined by imposing the Arrhenius law $K_i(T) = k_0 \exp\left(\frac{-E_A}{RT}\right)$. Apparent activation energies and frequency factors, calculated by linear regression of experimental data obtained by thermogravimetric measurements, are listed in Table 2. In order to account for mass transfer limitations inside the solid particle for varying particle diameter D the particle effectiveness factor η, experimentally determined by Trommer [19], is introduced:

$$\eta(D) = 0.571e^{-1.29\cdot10^4\cdot D} + 0.429e^{-9.56\cdot10^2\cdot D} \tag{23}$$

η converges to 1 for D approaching 0 and diffusion becoming instantaneous. Furthermore, comparison of the gasification rates between the experimental runs performed in the thermogravimeter (packed bed with heating rates of 0.1–0.3 K/s by predominantly convective/conductive heat transfer) and the experimental runs performed in the solar reactor (see next section; gas-particle flow with heating rates of 10^4–10^6 K/s by predominantly radiative heat transfer) led to the introduction of an empirical Arrhenius-type proportionality constant $k_{solar} = 498 \times \exp(-5.71 \times 10^4/RT)$ to resolve for the mass/heat transfer differences between both set-ups and the fact that the release of volatiles by pyrolysis occurs immediately at the entrance of the solar reactor. k_{solar} was obtained by numerical minimization of the difference between the gasification rates measured by thermogravimetry and those measured in the solar reactor [19].The volume specific reaction rate for specie i and for a single particle diameter D can then be written as:

$$R_i = k_{solar} \cdot r_i \cdot M_i \cdot Y_C \cdot \rho \cdot \eta(D) \tag{24}$$

For the polydisperse medium, η is evaluated at the equivalent monodisperse diameter D_η,

$$D_\eta = \eta^{-1}\left(\frac{\int_0^\infty f(D)D^3 \cdot \eta(D)\,dD}{\int_0^\infty f(D)D^3\,dD}\right) \tag{25}$$

where η^{-1} denotes the inverse function of Eq. (23).

4. Solar reactor configuration

A scheme of the reactor configuration is depicted in Fig. 1a. The details of its design and fabrication were presented previously [3]; only the main engineering features are highlighted here. It consists of a well-insulated 24-cm length 9.7-cm diameter cylindrical cavity-receiver, made of Inconel and lined with Al_2O_3, that contains a 5-cm diameter circular opening – the *aperture* – to let in concentrated solar radiation through a transparent quartz window. Petcoke-steam or petcoke-water slurry is injected at the front of the cavity and forms a particle-gas flow that progresses towards the rear of the cavity. With this arrangement, the coke particles are directly exposed to the high-flux solar irradiation, providing efficient heat transfer directly to the reaction site. Solar energy absorbed by the reactants is used to raise their temperature to above 1300 K and drive the gasification reaction. Experimentation was carried out at the PSI's solar furnace [20]: a 120 m^2 sun-tracking flat heliostat in-axis with a 8.5 m diameter paraboloidal concentrator, delivering peak solar concentration ratios exceeding 5000 suns (1 sun = 1 kW/m^2). Two experimental campaigns at a power level of 5 kW were performed: 1) "campaign 1", where petcoke particles and steam were injected separately [3]; 2) "campaign 2", where petcoke particles and water were injected together as a liquid slurry [4].

The model domain and the main boundary conditions are shown in Fig. 1b. Preliminary CFD simulations showed an axis-symmetric flow pattern with negligible radial velocity components. However, in order to account for the radial dependency of the incoming solar radiation, the domain is subdivided into concentric cylindrical compartments, as indicated in Fig. 1b. Advective heat transport is of secondary importance. Thus, a two-phase fluid flow with neglected circumferential and radial components of the velocity vector is assumed. This simplification further enables to

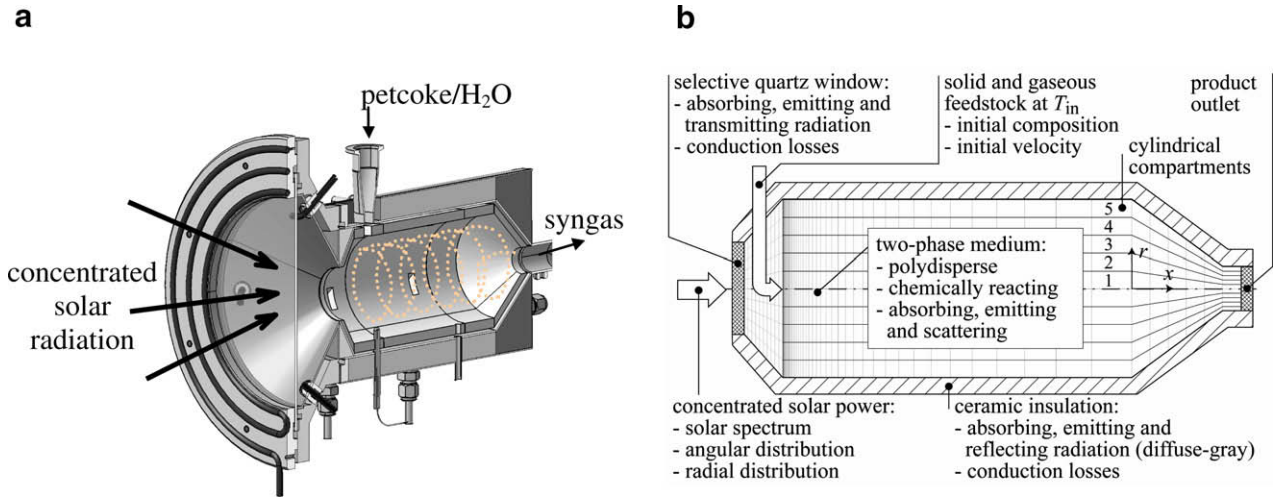

Fig. 1. (a) Scheme of solar chemical reactor configuration for the steam-gasification of carbonaceous materials (e.g. petcoke), featuring a continuous gas-particle vortex flow confined to a cavity receiver and directly exposed to concentrated solar radiation. (b) Axis-symmetric model domain, featuring five concentric cylindrical compartments. Indicated are also the boundary and inlet conditions.

better elucidate the physical phenomena involved in the interaction of radiation with the chemical reacting flow. The following boundary/initial conditions and material properties are set:

4.1. Concentrated solar radiation

The solar spectrum of the incoming radiation is approximated by Planck's blackbody emission at 5780 K. Fig. 2a shows the numerically modeled and the experimentally measured solar power through the aperture as a function of the aperture's radius. The data points correspond to the experimentally measured values, as recorded by a calibrated CCD camera on a water-cooled Al_2O_3-coated Lambertian target. The modeled results are calculated by a 3D Monte–Carlo raytracer that takes into account the exact geometry of the concentrating facility, specular reflection errors, and non-parallelism of the sun rays. Fig. 2b shows the calculated solar flux distribution and its angular distribution at the aperture, used as input to the solar reactor.

4.2. Quartz window

Spectral values for total transmittance, reflectance, and absorptance of the 3-mm thick quartz window are calculated using the Fresnel equations [14] based on the complex refractive index of quartz, plotted in Fig. 3 [21].

4.3. Reactor walls

Diffuse gray surfaces are assumed for the reactor's inner walls because of deposited petcoke particles. Convective heat transfer between the reactor walls and the fluid flow is found by CFD to be two orders of magnitude smaller than heat transfer by radiation and conduction, and is therefore neglected. Energy balance at the wall leads then to the following implicit expression for the temperature:

$$\int_0^\infty q''_{i,\lambda}\varepsilon_\lambda \,\mathrm{d}\lambda - \sigma\varepsilon T^4 - q''_{\text{conduction}} = 0 \tag{26}$$

where q''_i is the incident thermal radiation, the second term accounts for radiation emitted from the reactor walls, and the third term accounts for conduction heat losses through the walls:

$$q''_{\text{conduction}} = U\cdot(T_\infty - T_{\text{wall}}) \tag{27}$$

where the overall heat transfer coefficient U is based on 1D radial conduction through various layers of insulation of known thermal conductivities, as provided by the manufacturer.

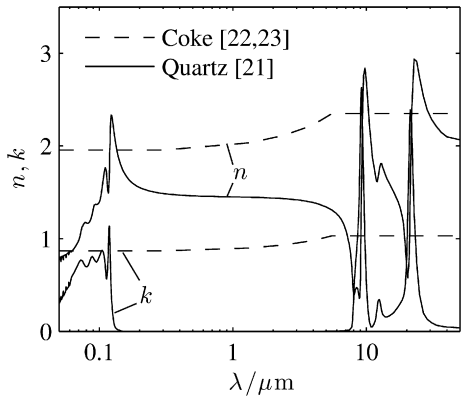

Fig. 3. Complex refractive index for petcoke and for quartz.

4.4. Feedstock injection

The inlet axial velocity is assumed to be uniformly distributed over the cross section, as found by preliminary CFD simulations and visual observation. Assuming ideal gas, the initial velocity is given by:

$$u_{\text{in}} = \frac{(\dot{n}_{H_2O} + \dot{n}_{Ar})\cdot R\cdot T_{\text{in}}}{p_0\cdot S} \tag{28}$$

where p_0 is the ambient pressure, S is the cavity cross-sectional area, and $\dot{n}_{H_2O}$ and $\dot{n}_{Ar}$ are the experimentally determined feeding rates of steam and argon, respectively. The inlet temperature T_{in} is equal to 423 K for campaign 1 and to the reactor's shell temperature for campaign 2.

4.5. Solid particles

Petrozuata Delayed coke was employed as feedstock (see Table 1). Values for its complex refractive index are shown in Fig. 3 [22,23]. Two particle size fractions were utilized. In campaign 1, the raw feedstock was ball and jet milled, and fed dry. In campaign 2, the raw feedstock was 80-μm screen sieved and fed as liquid slurry. Fig. 4 shows the volume density distribution, i.e. $f(D)\cdot D^3$, for both types of particles, as determined by laser scattering (Horiba LA950). Mean initial sizes are 2.21 and 17.58 μm for campaigns 1 and 2, respectively. As the chemical reaction progresses, $f(D)$ varies as a function of the carbon conversion X_C, defined in Eq. (35). Indicated in Fig. 4 are the resulting distributions for $X_C = 0$ (initial), 0.5, and 0.75. In principle, for Mie scattering, the absorption and scattering coefficients are calculated with Eq. (9). However, com-

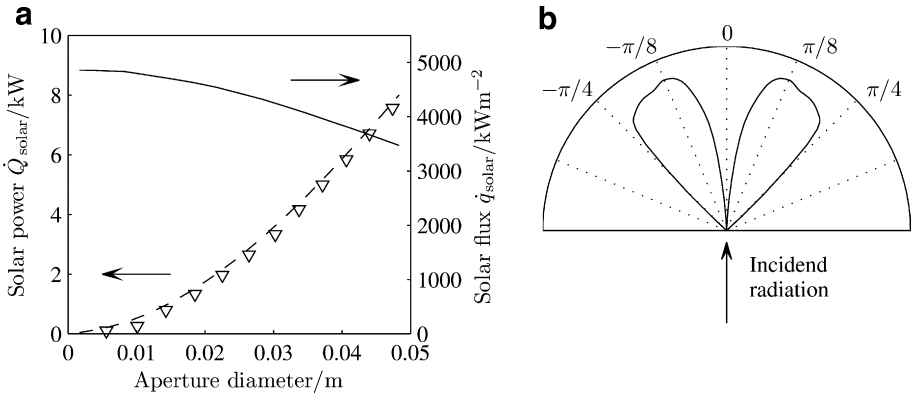

Fig. 2. (a) *Left axis*: variation of the numerically calculated (curve) and the experimentally measured (data points) solar power through the reactor's aperture as a function of the aperture's diameter. *Right axis*: calculated radial solar flux distribution at the aperture. (b) Angular distribution of the incoming radiation at the focal plane.

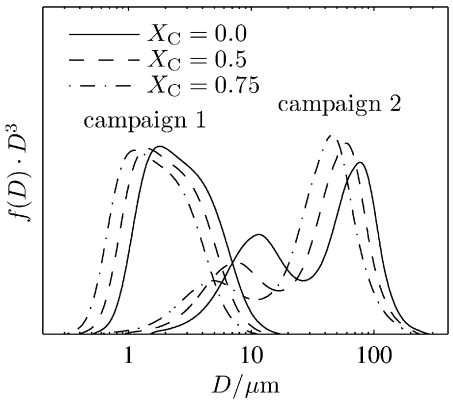

Fig. 4. Volume density of the polydisperse particles used in experimental campaigns 1 and 2. Solid lines are measured values for the unreacted samples, dashed and dashed-dotted lines are calculated values at carbon conversions of 0.5 and 0.75, respectively.

parison to the values calculated with the simplified approach of Eq. (10) showed negligible differences for the particle size distributions considered in this study. The polydisperse medium is therefore described by its equivalent diameters defined in Eqs. (2) and (25) without loss of information. D_{32}, D_{31}, D_{30} and D_η are shown in Fig. 5. The difference between the equivalent diameters indicate the importance of considering the polydisperse nature of the particulate medium, especially for the feedstock of campaign 2, where the difference reaches one order of magnitude. Note that D_{30} can be expressed in terms of the extent of carbon conversion by:

$$D_{30} = D_{30,\text{in}} \cdot (1 - X_C)^{\frac{1}{3}} \tag{29}$$

Figs. 6a and b shows the spectral absorption and scattering coefficients of the particulate medium in campaigns 1 and 2, respectively, for a typical initial volume fraction $f_v = 5 \times 10^{-5}$, and for carbon conversions $X_C = 0$, 0.5, and 0.75. The smaller particles of campaign 1 absorb more than 10 times better than those of campaign 2. The scattering phase function for particles of campaign 1 is shown in Figs. 7a and b for $X_C = 0.0$ and 0.75, respectively. Curves are plotted for a monodisperse particulate medium with equivalent diameter D_{32}, for the polydisperse particulate medium of Fig. 4, and for the Henyey–Greenstein (HG) approximation of Eq. (11). Preference for forward scattering is observed. As expected, the polydisperse particle cloud has a smoother scattering phase function, which is well approximated by the HG equation.

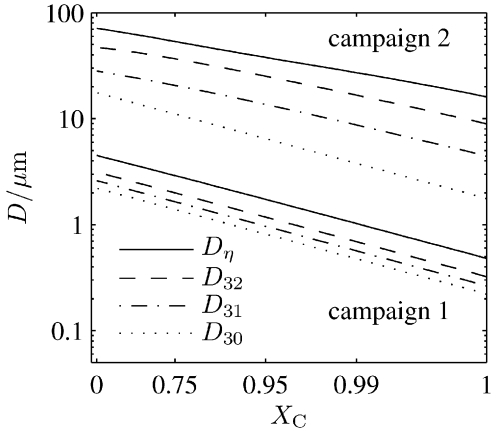

Fig. 5. Equivalent diameters calculated with Eqs. (2) and (25) of the polydisperse particles used in campaigns 1 and 2 as a function of the carbon conversion.

5. Numerical analysis

The domain is subdivided into finite volume elements with grid spacing adapted to the temperature gradient. Each element is considered isothermal (each phase separately), with homogenously distributed species and particle size fractions. The simulation is composed by two main coupled computational modules:

(1) A pathlength Monte–Carlo ray tracing module (MC) with ray redirection [24] for solving the equation of radiative transfer using the corresponding probability density functions for direction and wavelength of emission/scattering from particles and emission/reflection from boundary walls. For example, the wavelength of a generic ray emitted by the non-gray elemental medium is found by solving the implicit equation:

$$\Re_\lambda = \frac{\int_0^\lambda \kappa_\lambda e_{\lambda b}\,\mathrm{d}\lambda}{\int_0^\infty \kappa_\lambda e_{\lambda b}\,\mathrm{d}\lambda} \tag{30}$$

where $e_{\lambda b}$ is Planck's blackbody spectral emissive power evaluated at the temperature T of the location of emission and $\Re_\lambda$ denotes a random number drawn from a uniform distributed set between 0 and 1. Rays are generated by emission from the reactor inner walls, by emission by the elemental volumes (particle suspension), and by transmission through the window (incident $\dot{q}_{\text{solar}}$). Each ray can undergo three types of interactions: (1) absorption and scattering by the elemental volumes; (2) absorption, reflection, and transmission by the reactor walls and/or window; and (3) transmission to the adjacent volume element. The ray's history is terminated either when its power is diminished by subsequent absorption events below a set threshold, or when it exits the domain through the window.

(2) A finite-volume CFD module for solving the mass and energy conservation equations that link conduction/convection/radiation heat transfer to the chemical kinetics. Note that, because of statistical dispersion, the time required to perform a single iteration of the MC module at a reasonable accuracy is several orders of magnitude larger than that for the CFD module. To some extent this problem is alleviated by Gaussian kernel smoothing with adaptive bandwidth. For the incident radiation on the walls, the local mean estimator is expressed by Bowman and Azzalini [25]:

$$q''_{\text{in}}(x) = \frac{\sum_{i=1}^{n} w(x_i - x, h_i) \cdot q''_{\text{in,MC}}(x_i)}{\sum_{i=1}^{n} w(x_i - x, h_i)} \tag{31}$$

where $q''_{\text{in,MC}}$ denotes the result of the MC module, w is the Gaussian kernel defined as $w(x, h_i) = \exp(-x^2/2h_i^2)/h_i\sqrt{2\pi}$, and the bandwidth h_i is proportional to the local grid spacing. The divergence of the radiative flux is estimated analogously to Eq. (31), where a 2D kernel of the form $w(x_i - x, h_x) \cdot w(r_i - r, h_r)$ is used with bandwidths h_x and h_r proportional to the local grid spacing in the x and r direction, respectively [26]. An adaptive underrelaxation scheme for the radiative source term is introduced to ensure convergence and reduce the overall computational time:

$$\phi^i_{\text{radiation}} = (1 - \gamma^i) \cdot \phi^{i-1}_{\text{radiation}} + \gamma^i \cdot \phi^i_{\text{radiation,MC}} \tag{32}$$

$\phi^i_{\text{radiation,MC}}$ denotes the result of the MC module after the iteration step i, and γ is the adaptive underrelaxation factor. Ini-

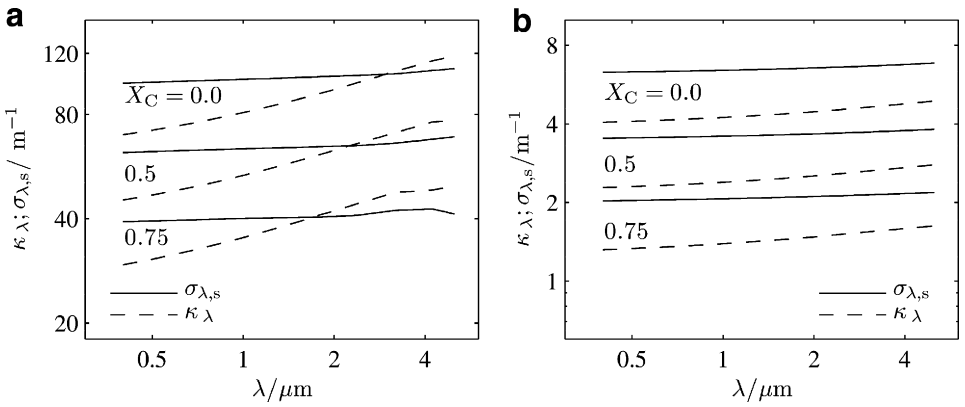

Fig. 6. Spectral distribution of the absorption and scattering coefficients, calculated for a typical volume fraction of 5×10^{-5} and carbon conversions of 0.0, 0.5, and 0.75, for the feedstock used in (a) campaign 1 and (b) campaign 2.

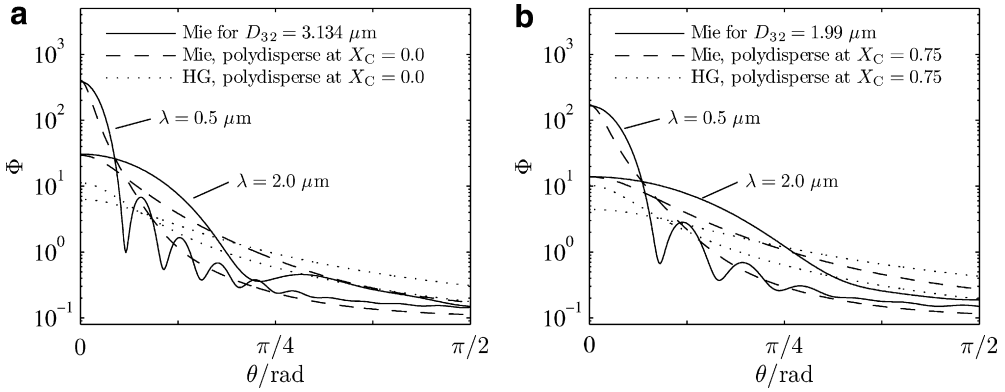

Fig. 7. Scattering phase function for the equivalent diameter D_{32} of the polydisperse medium (Eq. (12)), and for the Henyey–Greenstein approximation (Eq. (11)), calculated for carbon conversions of (a) 0 and (b) 0.75, for the feedstock used in campaign 1.

tially, γ is set to $\gamma^0 = 1$ and the radiative source term is calculated with low accuracy but relatively fast. Once convergence is reached, γ is subsequently reduced according to:

$$\gamma^i = \gamma^0 \exp\left(\frac{i_0 - i}{\xi}\right) \tag{33}$$

where i_0 is the iteration step for the system convergence and ξ is a positive real number. Fig. 8 shows the development of the relative RMS error for the particle temperature, $RMS = \left(\sum_1^n ((T^{i+1} - T^i)/T^{i+1})^2/n\right)^{1/2}$. A MC simulation with only 2×10^4 primary rays results in convergence after 150 iterations, yielding a standard deviation of 0.12 and 0. 07 for the raw and the smoothed $\phi_{\text{radiation}}$, respectively. Significant increase in accuracy is accomplished by reduction of γ beyond iteration step $i_0(\xi = 32)$. In principle, accuracy could also be enhanced by increasing the number of rays in the MC module but at the expense of dramatically increasing computational time. For example, a typical MC simulation requires 3, 26, and 258 s for 10^4, 10^5, and 10^6 primary rays with a corresponding standard deviation for $\phi_{\text{radiation}}$ of 0.13, 0.04, and 0.015, respectively.

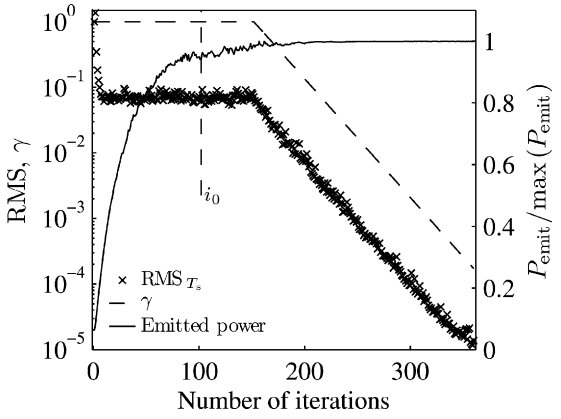

Fig. 8. *Left axis*: relative RMS error for the solid temperature and underrelaxation parameter γ as function of the iteration number. *Right axis*: total emitted power, normalized by its maximal value, used as an indicator for system convergence.

6. Numerical results and experimental validation

Sets of 23 and 20 solar experimental runs were carried out for campaigns 1 and 2, respectively. Numerically simulated and experimentally measured cavity and reactor shell temperatures, and carbon/steam conversions at the reactor outlet are shown in Fig. 9 for (a) campaign 1; and (b) campaign 2. T_{cavity} for the experimental runs is the mean between the pyrometer reading corrected for window transmittance and the thermocouple reading T_{shell} corrected for conduction through the reactor walls. T_{cavity} for the numerical simulation is the weighted mean over all finite volumes of the cavity, $T_{\text{cavity}} = \sum T_i V_i \rho_i / \sum V_i \rho_i$ while the lower and upper error bars describe the 25th and 75th percentile of T_i, respectively.

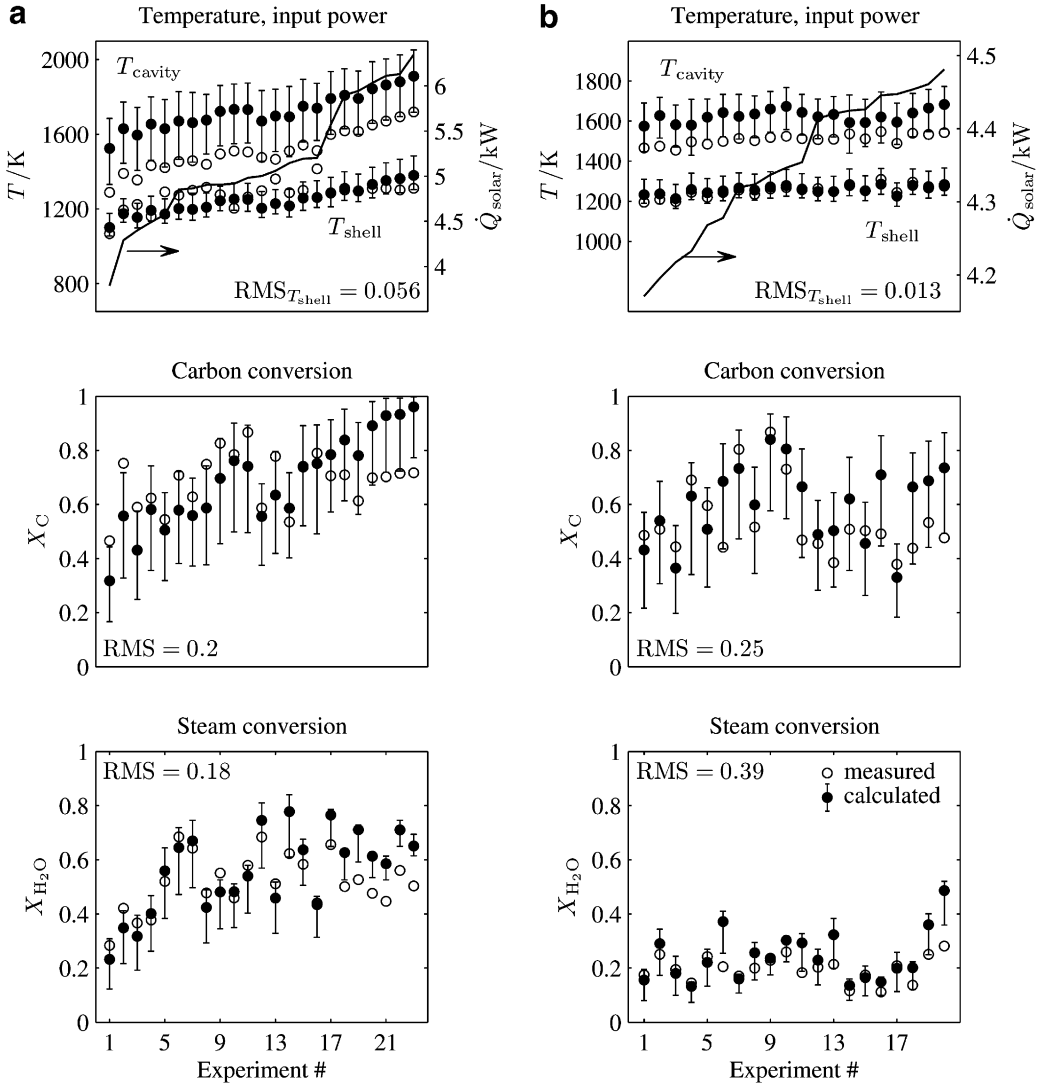

Fig. 9. Numerically calculated and experimental measured data for the (a) 23 solar experimental runs of campaign 1; and (b) 20 solar experimental runs of campaign 2, ordered by increasing $\dot{Q}_{\text{solar}}$. Shown are the average cavity and wall temperatures, and the carbon and steam conversions at the outlet. Dots and crosses indicate numerically calculated values; circles and triangles indicate the experimentally measured data; the bars indicate the propagated error of the input parameters.

Steam and coke conversions are determined from the oxygen and carbon mass balance[1]:

$$X_{H_2O} = \frac{\dot{n}_{CO} + 2 \cdot \dot{n}_{CO_2}}{\dot{n}_{H_2O,in}} \tag{34}$$

$$X_C = \frac{\dot{n}_{CO} + \dot{n}_{CO_2} + \dot{n}_{CH_4}}{\dot{n}_{C,in}} \tag{35}$$

The error bars for the calculated values are due to the propagated error of the input parameters, namely ±5% for the coke feeding rate and $\pm^{9\%}_{13\%}$ for the solar power input, caused mainly by the heliostat tracking error and misalignment [3]. Relative RMS errors for T_{shell}, X_{H_2O}, and X_C were 5.6%, 20%, and 18%, respectively, in campaign 1, and 5.4%, 25%, and 39%, respectively, in campaign 2. Overlapping of the accuracy intervals (error bars) of calculated and measured data points is observed for the majority of the experiments. Calculated temperature ranges for T_{cavity} are found to be significantly

[1] The gaseous products were analyzed on-line by gas chromatography (GC, High speed Micro GC G2890A by Agilent Technologies, equipped with molecular sieve 5A and HaySep A capillary columns), IR-based detectors for CO, CO_2, and CH_4 (Ultramat-23 by Siemens), and a thermal conductivity-based detector for H_2 (Calomat-6 by Siemens).

Table 3
Baseline model parameters for two representative solar experimental runs for campaigns 1 and 2

Experimental campaign #			1	2
Molar inlet flow rates	$\dot{n}_C$	mol/min	0.254	0.102
	$\dot{n}^1_{H_2}$	mol/min	0.142	0.057
	$\dot{n}_{H_2O}$	mol/min	0.446	0.264
	$\dot{n}_{Ar}$	mol/min	0.266	0.165
Overall H_2O:C ratio		–	1.76	2.6
Inlet velocity	u_{in}	m/s	0.065	0.088
Solar power input	$\dot{Q}_{solar}$	kW	5.7	4.7
Static pressure	p_0	Pa	10^5	
Inlet equivalent particle diameter	$D_{30,in}$	μm	2.21	17.58
	$D_{32,in}$	μm	3.13	47.14
Inlet temperature	T_{in}	K	423.15	
1003.5				
Reactor cross sectional area	S	m^2	$8 \cdot 10^{-3}$	
Overall heat transfer coefficient	U	W/(m^2K)	25	
Outer temperature of the reactor shell	T_∞	K	593.15	

[1] bound in the feedstock.

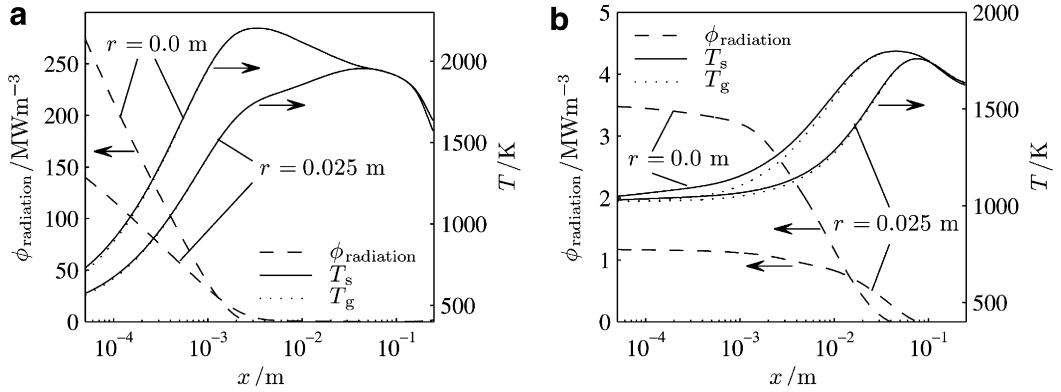

Fig. 10. Numerically calculated temperature profiles for the gaseous and solid phases, and the radiative source term along the reactor at two radial positions: center (r = 0 m) and close to the wall (r = 0.025 m). The baseline parameters listed in Table 3 were employed for (a) campaign 1; and (b) campaign 2.

higher than those experimentally measured, especially for campaign 1, in which peak temperatures occur at the center of the cavity due to strong radiation absorption by small particles. Table 3 lists the selected baseline model parameters of two representative solar experimental runs for each experimental campaign [3,4]. Fig. 10 shows the temperature profiles for the gaseous and solid phases and the radiative source term along the reactor calculated for the baseline parameters listed in Table 3 at two radial positions: center (r = 0 m) and close to the wall (r = 0.025 m). Note that the x-axis scale is logarithmic for a better appreciation of the rapid heating rate – of the order of 10^5 K/s – during the first centimeters after the inlet plane, where particles reach temperatures of 2144 and 1861 K for campaigns 1 and 2, respectively. Thus, very efficient radiative heat transfer to the reactants is attained by direct concentrated irradiation of the gas-particle flow. Temperatures peak after 1 and 5 cm for campaigns 1 and 2, respectively, and decrease towards the rear of the reactor as a result of the endothermic reaction and conductive heat losses. As expected from the time scales $\tau_{convection}$ *and* $\tau_{radiation}$, the temperature difference between the solid and gas phases is negligible for campaign 1 with smaller particles, and less than 50 K for campaign 2 with bigger particles. The mean temperature of the metallic shell T_{shell} is in the range 1108–1301 K and significantly below that of the coke particles because of the Al_2O_3 liner and because the particle suspension serves as a radiation shield, as corroborated experimentally in a similar gas-particle reactor configuration [10]. The radiation source term undergoes a fast decrease as the reactants flow along the reactor because of two congruent phenomena: (1) the absorption coefficient of the particle suspension rapidly decreases with increasing temperatures due to volumetric expansion, and (2) particles shrink and disappear as the reaction progresses, thus lowering the net radiation transmitted. A strong radial temperature gradient is induced by the angular and radial distribution of the incoming solar radiation, but this gradient diminishes after approximately 10 cm behind the aperture as a result of absorption by the particles and emission from particles and walls.

The progress of the chemical reaction is shown in Fig. 11, where the variation of the chemical composition (molar fractions) is plotted along the reactor at two radial positions: center (r = 0 m) and close to the wall (r = 0.025 m). The baseline parameters of campaigns 1 and 2, listed in Table 3, were employed. Note that the x-scale is shown linear – and not logarithmic as in Fig. 10, as the chemical reaction rates are significantly slower than the radiative heat transfer rates. Main product gas components are H_2 and CO, with less than 5% CO_2, as predicted by thermodynamic equilibrium [2]. Simultaneous fast pyrolysis and steam-gasification occurs immediately after the entrance of the reactor. The steam and carbon conversions are significantly lower close to the walls that those obtained at the center line as a result of the relatively low temperatures existing there. In addition, reaction rates decrease towards the exit of the reactor, primarily because of the lower temperatures attained for a decreasing radiation source, as indicated in Fig. 10b. As expected, the gasification proceeds at a higher rate in campaign 1, due to the higher temperatures and particle effectiveness factor η of the feedstock. This is also corroborated in the 2D contour maps of Fig. 12, showing the reaction rate $\partial X_C/\partial t$ and the carbon conversion X_C in the upper plot – normalized with its maximal value –, and the corresponding temperature profiles in the lower plot. In campaign 1, the peaks for the temperature (>2050 K) and for $\partial X_C/\partial t$ (1.4×10^5 s^{-1}) are pronounced and located in the first centimeters after the inlet plane, followed by a decrease to 1800 K and 6×10^{-6} s^{-1}, respectively, towards the exit of

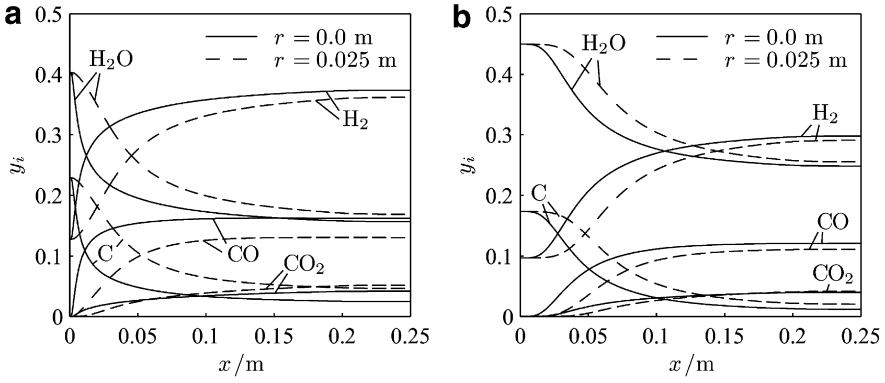

Fig. 11. Variation of the chemical composition (molar fractions) along the reactor at two radial positions: center (r = 0 m) and close to the wall (r = 0.025 m). The baseline parameters listed in Table 3 were employed for (a) campaign 1 and (b) campaign 2.

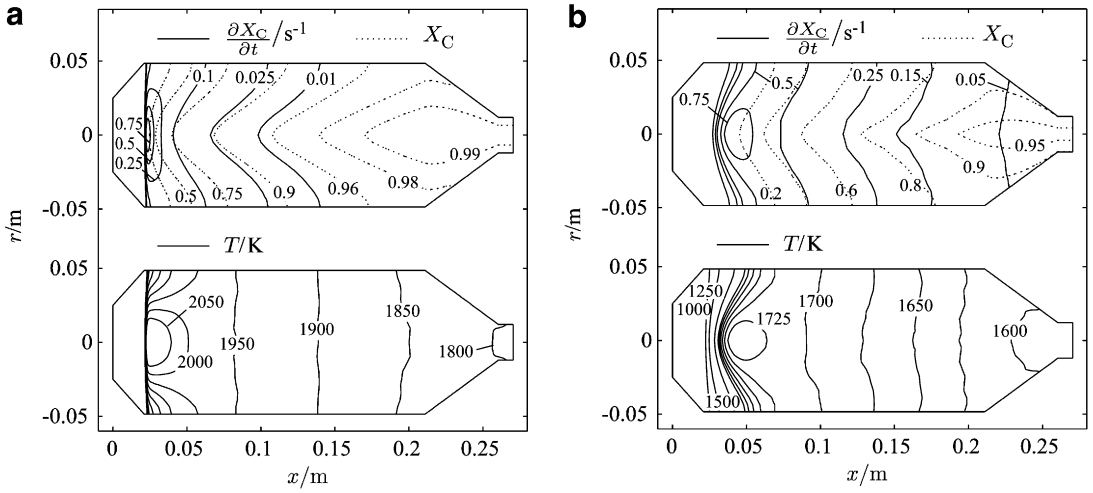

Fig. 12. 2D contour map of the carbon conversion X_C and reaction rate dX_C/dt (upper plot) and corresponding temperatures (lower plot). The baseline parameters listed in Table 3 were employed for (a) campaign 1 and (b) campaign 2.

the reactor. In campaign 2, a more uniform temperature and reaction rate field is observed, with maximum values attained 5 cm after the inlet plane. The difference between the two campaigns is attributed to the differences in the particle sizes of their feedstock. The smaller particles used in campaign 1 have a higher absorption coefficient, as observed in Fig. 6, augmenting radiative heat transfer at the entrance region but preventing radiation to penetrate deeper into the rear of the cavity. The smaller H_2O:C molar ratio, and consequently, the higher solid volume fraction, further contributes to this effect. For example, at the location of maximum temperature, $f_v = 1.83 \times 10^{-5}$ and 9.75×10^{-6}, and the corresponding absorption coefficient $\kappa = 13.3$ and $0.28\ m^{-1}$, for campaigns 1 and 2, respectively. At the exit of the reactor, after condensing the unreacted and excess H_2O, the molar composition of the syngas was 0.66 H_2: 0.25 CO: 0.09 CO_2 for campaign 1 and 0.68 H_2: 0.21 CO: 0.11 CO_2 for campaign, which compares well with the gas composition measured experimentally [3,4]. Finally, a sensitivity analysis is performed to elucidate the effect of a given input parameter Z by computing the system derivative $S_i = \partial Y/\partial Z$, where Y is the output of interest [27]. The input parameters are the solar power input $\dot{Q}_{solar}$, the coke feeding rate $\dot{n}_C$, and the inlet temperature T_{in}. The outputs of interest are the mean reactor temperature $T_{reactor}$ and the carbon conversion at the reactor outlet. Results are listed in Table 4, where $S_{i,relative}$ is the local relative sensitivity defined as $S_{i,relative} = \frac{[Y(Z+\frac{\Delta Z}{2}) - Y(Z-\frac{\Delta Z}{2})]/Y}{\Delta Z/Z}$ with $\Delta Z/Z = 0.05$. $\dot{Q}_{solar}$ is the input parameter with the strongest impact on the output, especially on for both campaigns. For campaign 1, increasing $\dot{n}_C$ has a negative impact on X_C and $T_{reactor}$. Interestingly, for campaign 2, its impact on $T_{reactor}$ is positive because the feedstock is introduced at a much higher temperature after preheating T_{in} has a positive impact for both campaigns, but stronger for campaign 2. An increase in the inlet temperature compensates for the weaker radiation absorption by the feedstock used in campaign 2 because it reduces the energy required to heat the reactants to the reaction temperature and, consequently, increases the energy left to drive the chemical reaction.

Table 4
Relative sensitivity of input/output parameters for both experimental campaigns

Campaign	Z→	$\dot{Q}_{solar}$	$\dot{n}_C$	T_{in}
1	$S_{relative}(T_{reactor})$	0.42	−0.090	0.026
1	$S_{relative}(X_C)$	1.46	−0.41	0.073
2	$S_{relative}(T_{reactor})$	0.31	0.014	0.11
2	$S_{relative}(X_C)$	1.81	−0.16	0.40

7. Summary and conclusion

We have developed a heat and mass transfer model for a polydisperse particle suspension subjected to concentrated thermal radiation and undergoing an endothermic chemical transformation. The model was applied in the simulation of a solar reactor for the steam-gasification of carbonaceous materials. Energy and mass conservation equations were formulated for each phase and species in a multi-compartment domain, and solved by 3D Monte–Carlo and finite volume techniques. Chemical kinetics was modeled by means of a set of Langmuir–Hinshelwood type rate laws, with Arrhenius rate constants determined by thermogravimetry. Numerical results for average temperatures, carbon and steam conversions, and gas compositions at the reactor outlet agreed well to those obtained in two experimental campaigns carried out with a 5 kW solar reactor prototype in a high-flux solar furnace. Heating rates of 10^5 K/s were obtained as a result of the efficient radiative heat transfer. The different particle size distribution of the feedstock employed in the two campaigns affected strongly the absorption coefficient and chemical kinetics, and consequently mass and heat transfer, justifying the detailed analysis of the polydisperse medium.

Acknowledgements

This study was conducted within the framework of a joint PDVSA-CIEMAT-ETH project aimed at developing the chemical reactor technology for the solar gasification of petcoke. We thank P. Haueter and D. Trommer from ETH Zurich, M. Romero from CIEMAT, and J.C. de Jesus from PDVSA for the experimental data obtained during the experimental campaign at PSI's solar furnace.

References

[1] A. Steinfeld, Solar thermochemical production of hydrogen – a review, Solar Energy 78 (5) (2005) 603–615.
[2] D. Trommer, F. Noembrini, M. Fasciana, D. Rodriguez, A. Morales, M. Romero, A. Steinfeld, Hydrogen production by steam-gasification of petroleum coke using concentrated solar power – I. Thermodynamic and kinetic analyses, International Journal of Hydrogen Energy 30 (2005) 605–618.
[3] A. Z'Graggen, P. Haueter, D. Trommer, M. Romero, J.C. de Jesus, A. Steinfeld, Hydrogen production by steam-gasification of petroleum coke using

concentrated solar power – II. Reactor design, testing, and modeling, International Journal of Hydrogen Energy 31 (2006) 797–811.
[4] A. Z'Graggen, P. Haueter, G. Maag, A. Vidal, M. Romero, A. Steinfeld, Hydrogen production by steam-gasification of petroleum coke using concentrated solar power – III. Reactor experimentation with slurry feeding, International Journal of Hydrogen Energy 32 (2007) 992–996.
[5] L.A. Dombrovsky, W. Lipinski, A. Steinfeld, A diffusion-based approximate model for radiation heat transfer in a solar thermochemical reactor, Journal of Quantitative Spectroscopy & Radiative Transfer 103 (2007) 601–610.
[6] J. Marakis, C. Papapavlou, E. Kakaras, A parametric study of radiative heat transfer in pulverized coal furnaces, International Journal of Heat and Mass Transfer 43 (2000) 2961–2971.
[7] W. Lipiński, A. Z'Graggen, A. Steinfeld, Transient radiation heat transfer within a nongray nonisothermal absorbing–emitting–scattering suspension of reacting particles undergoing shrinking, Numerical Heat Transfer, Part B: Fundamentals 47 (2005) 443–457.
[8] W. Lipinski, A. Steinfeld, Transient radiative heat transfer within a suspension of coal particles undergoing steam gasification, Heat Mass Transfer 41 (2005) 1021–1032.
[9] P.v. Zedtwitz, A. Steinfeld, Steam-gasification of coal in a fluidized-bed/packed-bed reactor exposed to concentrated thermal radiation – modeling and experimental validation, Industrial & Engineering Chemistry Research 44 (2005) 3852–3861.
[10] P.v. Zedtwitz, W. Lipiński, A. Steinfeld, Numerical and experimental study of the gas-particle radiative exchange for the steam-gasification of coal, Chemical Engineering Science 62 (1) (2007) 599–607.
[11] D. Hirsch, A. Steinfeld, Radiative transfer in a solar chemical reactor for the Co-production of hydrogen and carbon by thermal decomposition of methane, Chemical Engineering Science 59 (2004) 5771–5778.
[12] F.P. Incropera, D.P. DeWitt, Fundamentals of Heat and Mass Transfer, John Wiley & Sons, New York, 2002.
[13] L.S. Rothman et al., The HITRAN molecular spectroscopic database and HAWKS (HITRAN atmospheric workstation): 1996 edition, Journal of Quantitative Spectroscopy & Radiative Transfer 60 (1998) 665–710.
[14] R. Siegel, J. Howell, Thermal Radiation Heat Transfer, Taylor & Francis, New York, 2002.
[15] M. F Modest, Radiative Heat Transfer, Academic Press, Amsterdam, 2003.
[16] C.F. Bohren, D.R. Huffman, Absorption and Scattering of Light by Small particles, Wiley, New York, 1983.
[17] L.G. Henyey, J.L. Greenstein, Diffuse radiation in the galaxy, Astrophysical Journal 88 (1940) 70–83.
[18] D. Trommer, A. Steinfeld, Kinetic modeling for the combined pyrolysis and steam-gasification of petroleum coke and experimental determination of the rate constants by dynamic thermogravimetry in the 500–1520 K range, Energy & Fuels 20 (2006) 1250–1258.
[19] D. Trommer, Thermodynamic and Kinetic Analyses of Solar Thermal Gasification of Petroleum Coke, Ph.D. thesis, ETH Zurich, 2006.
[20] P. Haueter, T. Seitz, A. Steinfeld, A new high-flux solar furnace for high-temperature thermochemical research, Journal of Solar Energy Engineering 121 (1999) 77–80.
[21] E.D. Palik, Handbook of Optical Constants of Solids, Academic Press, 1985.
[22] L.D. Burak, Radiaitve properties of coke particles of coal-dust flame, Inzhenerno-Fizicheskii Zhurnal 45 (1983) 297–302.
[23] F. Goodarzi, Optical properties of vitrinite carbonized at different pressures, Fuel 64 (1985) 156–162.
[24] T.F. Irvine Jr., J.P. Hartnett, Advances in Heat Transfer, vol. 31, Academic Press, 1998. pp. 333–429.
[25] A.W. Bowman, A. Azzalini, Applied Smoothing Techniques for Data Analysis The Kernel Approach with S-Plus Illustrations, Clarendon Press, 1997.
[26] D. Ruppert, M.P. Wand, Multivariate locally weighted least squares regression, The Annals of Statistics 22 (1994) 1346–1370.
[27] A. Saltelli, Sensitivity Analysis in Practice a Guide to Assessing Scientific Models, Wiley, 2004.